Photoacoustic–Ultrasound Tomography With S-Sequence Aperture Encoding

Quinn M. Barber, *Associate Member, IEEE*, and Roger J. Zemp, *Member, IEEE*

***Abstract*— A combined photoacoustic–ultrasound (PAUS) tomography system is introduced using ring-array and novel aperture encoding schemes. The ultrasound subsystem is able to achieve diffraction limited half-wavelength isotropic in-plane spatial resolution unlike previous systems. S-sequence aperture encoding improves signal-to-noise ratio (SNR) for the ultrasound tomography (UST) subsystem. We measured an average resolution of 139 ± 44 μm for S-sequence UST and a resolution of 180 ± 32 μm for photoacoustic tomography. We were able to measure SNR improvement using S-sequence spatial encoding using tissue-mimicking phantoms, and we displayed a composite PAUS phantom image.**

***Index Terms*— Medical imaging, photoacoustics.**

I. Introduction

PHOTOACOUSTIC tomography (PAT) is an emerging hybrid imaging modality that provides optical absorption contrast with scalable ultrasonic spatial resolution [1]–[3]. Combined ultrasound and photoacoustic imaging is attractive as ultrasound provides structural context to the functional and molecular information provided by photoacoustic images [4]–[7]. PAT has been implemented in many form factors, including linear arrays [8], [9], ring-transducer arrays [10]–[13], and bowl-shaped detector geometries [14], [15]. Ring and bowl-shaped array geometries mitigate limited view artifacts associated with linear arrays. Despite many previous works regarding ultrasound transmission and reflection tomography [16]–[21] and PAT [1], [12], [13], [22]–[25], a combined system that achieves the ultrasonic diffraction limit has yet to be presented. The goal of this paper is to introduce such a system and present an aperture encoding scheme to improve the signal-to-noise ratio (SNR) of the ultrasound tomography (UST) images and automatically coregister with PAT images.

Recently, high-frequency ultrasound–photoacoustic imaging systems have seen commercialization [26], [27]. Lateral and axial resolutions of 30 μm for 30–70-MHz transducers (with center frequencies around 50 MHz) provide detailed structural views for preclinical imaging applications [28], [29]. Tissue penetration, however, becomes much more challenging at higher frequencies. Photoacoustic–ultrasound (PAUS) tomography with ring arrays has recently been introduced and promises isotropic in-plane resolution with a theoretical resolution limit of $\sim$150 μm for a 5-MHz array. This resolution is comparable with high-frequency array systems, but enables deeper penetration and potentially higher sensitivity to large objects as photoacoustic signal frequency content is related to absorber size.

In the past few years, Merčep *et al.* [20], [26] have developed a reflection-mode PAUS tomographic system using the synthetic transmit aperture (STA) technique with a 2-D limited-view ring array. They utilized incoherent image compounding to boost their SNR; however, this reduced the theoretical resolution of their system to 2x that dictated by the diffraction limit [20].

We introduce a PAUS tomography system that uses coherent, rather than incoherent, synthetic aperture compounding to meet the theoretical half-wavelength diffraction limit for ultrasound. Gemmeke and Ruiter [30] implemented such coherent STA reconstruction, but did not implement PAT. One cost of the synthetic aperture approach, also seen in [30], is the limited SNR associated with transmitting on only one element at a time. To overcome this SNR challenge, we implement an S-sequence aperture encoding technique previously introduced for linear arrays [31]. This technique will allow us to boost our SNR by $\log_{10}(M+1)-1.5$ dB [32] without degrading our spatial resolution. In this paper, we will describe the theory and implementation of S-sequence encoding and confirm that it will not affect the resolution of our system. Then, we will measure SNR improvement in UST using simple targets and tissue-mimicking phantoms. Finally, a composite PA-UST image will be presented.

II. Theory: S-Sequence Encoding

Spatial encoding for ultrasound arrays involve applying a weighting mask w_j^i on each transmitting element j for each transmit event i. After this weighting is applied for one transmit event, the observed signal $p_k^i(t)$ can be described as

$$\begin{bmatrix} p_1^i(t) \\ p_2^i(t) \\ \vdots \\ p_N^i(t) \end{bmatrix} = \begin{bmatrix} e_{11}(t) & e_{12}(t) & \cdots & e_{1N}(t) \\ e_{21}(t) & e_{22}(t) & \cdots & e_{2N}(t) \\ \vdots & \vdots & \ddots & \vdots \\ e_{N1}(t) & e_{N2}(t) & \cdots & e_{NN}(t) \end{bmatrix} \begin{bmatrix} w_1^i \\ w_2^i \\ \vdots \\ w_N^i \end{bmatrix} + \begin{bmatrix} n_1(t) \\ n_2(t) \\ \vdots \\ n_N(t) \end{bmatrix} \tag{1}$$

where $e_{\mathrm{kj}}(t)$ is defined as the received signal of element k from pulsing transmit element j and $n_k^i(t)$ is zero-mean additive

Manuscript received November 10, 2016; accepted January 24, 2017. Date of publication January 30, 2017; date of current version April 1, 2017. This work was supported in part by the Natural Sciences and Engineering Research Council of Canada under Grant NSERC RGPIN 355544 and Grant CHRPJ 462510, in part by the Canadian Institutes of Health Research under Grant CIHR CPG 134739, and in part by the Canadian Cancer Society under Grant CCS 2011-700718.

The authors are with the Electrical and Computer Engineering Department, University of Alberta, Edmonton, AB T6G 2R3, Canada (e-mail: zemp@ualberta.ca).

Digital Object Identifier 10.1109/TUFFC.2017.2661238

noise. For M transmit events, this matrix can be expanded to

$$\begin{bmatrix} p_1^1(t) & p_1^2(t) & \cdots & p_1^M(t) \\ p_2^1(t) & p_2^2(t) & \cdots & p_2^M(t) \\ \vdots & \vdots & \ddots & \vdots \\ p_N^1(t) & p_N^2(t) & \cdots & p_N^M(t) \end{bmatrix} = \begin{bmatrix} e_{11}(t) & e_{12}(t) & \cdots & e_{1N}(t) \\ e_{21}(t) & e_{22}(t) & \cdots & e_{2N}(t) \\ \vdots & \vdots & \ddots & \vdots \\ e_{N1}(t) & e_{N2}(t) & \cdots & e_{NN}(t) \end{bmatrix} \begin{bmatrix} w_1^1 & w_1^2 & \cdots & w_1^M \\ w_2^1 & w_2^2 & \cdots & w_2^M \\ \vdots & \vdots & \ddots & \vdots \\ w_N^1 & w_N^2 & \cdots & w_N^M \end{bmatrix} + \begin{bmatrix} n_1^1(t) & n_1^2(t) & \cdots & n_1^M(t) \\ n_2^1(t) & n_2^2(t) & \cdots & n_2^M(t) \\ \vdots & \vdots & \ddots & \vdots \\ n_N^1(t) & n_N^2(t) & \cdots & n_N^M(t) \end{bmatrix}.$$

This can be written in matrix form

$$\mathbf{P}(t) = \mathbf{E}(t)\mathbf{W} + \mathbf{n}(t). \tag{2}$$

In this context, STA imaging could be achieved if $\mathbf{W}$ was equal to an identity matrix; in other words, $\mathbf{P}(t) = \mathbf{E}(t)$. Thus, when using a more complex weighting matrix, STA image data can be recovered by calculating $\hat{\mathbf{E}} = \mathbf{P}(t)\mathbf{W}^{-1}$. By choosing a $\mathbf{W}$ that uses transmits on more than one element per transmit event, the SNR can be increased by increasing the total energy per event. Consequently, for spatial encoding, it is important to use a $\mathbf{W}$ that maximizes SNR improvement while minimizing error due to inversion. Suitable inversion error can be determined by finding a weighting matrix with $(\epsilon/\sigma^2) = tr[\mathbf{W}^{-1}(\mathbf{W}^{-1})^{\mathsf{T}}]$ that is as small as possible, where σ^2 is the variance of the noise and $\epsilon = \langle(\hat{\mathbf{E}} - \mathbf{E})(\hat{\mathbf{E}} - \mathbf{E})^{\mathsf{T}}\rangle$ and $\hat{\mathbf{E}} = \mathbf{P}(t)\mathbf{W}^{-1}$ is the recovered signal [32].

A popular weighting fitting this description is the Hadamard matrix [32]. For an $M \times M$ Hadamard matrix $\mathbf{H}_{2^N}$ (where $M = 2^N$), $(\epsilon/\sigma^2) = M + 1$, which is acceptable [32]. It can be easily calculated using the Sylvester construction technique, and easily inverted, where $\mathbf{H}_{2^N}^{-1} = (1/2^N)\mathbf{H}_{2^N}$ [32]. The resulting noiseless SNR gain can be calculated as $10\log_{10}(M)$ (due to the fact that M times more transmit pulses are used per transmit event). The elements within this matrix are equal to either -1 or 1, and thus it is dependent on the creation of a pulse that is an exact inverted copy of a positive pulse. In practice, this is difficult; for any inconsistencies between the inverted and positive pulses, it will severely degrade the efficacy of the inversion [32]. Therefore, we seek a weighting matrix that avoids the necessity of inverted pulses.

In this paper, we propose to use an S-matrix, a matrix derived from the Hadamard matrix made up of 1s and 0s. S-matrices ($\mathbf{S}_{2^N-1}$) of order $M = 2^N - 1$ are constructed by removing the first row and column of a Hadamard matrix $\mathbf{H}_{2^N}$, and replaces instances of 1s by 0 and instances of -1s by 1. Although this removes the necessity of inverted pulses, the nonzero elements per transmit event are halved. This will reduce the theoretical SNR improvement to $10\log_{10}(M+1) - 1.5$ dB, only 1.5 dB less than the Hadamard. Regardless, the S-matrix inversion condition is $(\epsilon/\sigma^2) = [2 - 2/(M+1)]^2$, which is acceptable. It can also be easily inverted: $\mathbf{S}_{2^N-1}^{-1} = (1/2^N)2\mathbf{S}_{2^N-1}^{\mathsf{T}} - \mathbf{J}$, where $\mathbf{J}$ is an appropriately sized matrix of 1s.

Because the S-matrix avoids the difficulty of implementing inverted pulses with negligible SNR decrease, we opt to use this weighting matrix for our spatial encoding, which will heretofore be referred to as S-sequence spatial encoding. This was applied in [31] for linear array imaging, but we illustrate its utility for improving SNR for UST.

III. Methods and Materials

A 5-MHz 256-element 256° ring array was used for our experiments (Imasonic SAS, France). Each element had a pitch of 0.7 mm, an interelement spacing of 0.1 mm, and a height of 10 mm. The bandwidth of this array was 55%, and toroidal elevation focusing has been applied. The elements themselves have been impedance matched to water. A Verasonics VDAS I ultrasound acquisition system (Verasonics, Inc., Redmon, WA, USA) was used in conjunction with this transducer. This system can transmit on 256 elements, and receive on 128. We used a sampling rate of 20 MHz. The raw data collected were postprocessed using MATLAB (The MathWorks, Inc., Natick, MA, USA). For the PA images, a 532-nm 10-Hz laser was used (Surelite Continuum III). Light was delivered through a ten-legged fiber bundle (CeramOptec) situated around the transducer to produce a thin strip of illumination on the target. The laser fluence used in our experiments was set to 20 mJ/cm^2. The setup schematic can be seen in Fig. 1.

To implementing S-sequence spatial encoding, the rows of the S-matrix were used as an apodization function for the transmit elements. The resulting received signal is then decoded by multiplying it with the inverted S-matrix, recovering our STA image data. Due to issues caused by crosstalk between elements, only 63 elements were used for transmission, utilizing every fourth element in the array. Acquisition of data achieved a speed of $\sim$ 150 frames/s for both STA and S-sequence methods when using 64 elements. For 50x averaging, acquisition of data reduced to 1 frame/s. Thus, this amount of averaging can be done within a breath hold. Averaging was done before coherent compounding, but could also be done after, which may offer improved robustness to motion, a point that needs to be researched in the future. Data were transferred then decoded and reconstructed offline. An addition of parallel computing schemes and implementation of graphical processing units could allow real-time reconstruction rates; however, this is left to future work [17], [33].

To reconstruct UST images, we implemented a delay-and-sum technique: distances were calculated from a receive element to the chosen pixel, and back to the transmitting element. Assuming a constant speed of sound, these distances were converted to time delays, allowing the appropriate signal information to be backpropagated to the respective pixel. The unscattered transmitted ultrasound signals, which propagate directly through the object, were removed from the received signal before backpropagation. The signal was then corrected for signal losses due to distance. Appropriate time gain compensation was then applied. This was repeated for each receive element and then for each transmit event. As the reconstruction

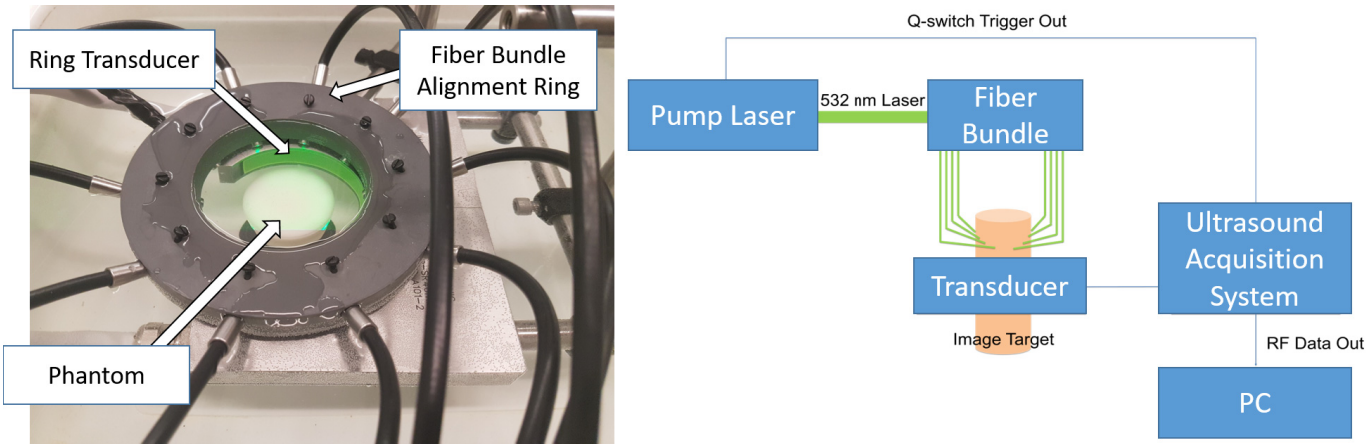

Fig. 1. Schematic of UST and PAT system.

will contain both positive and negative signals, we chose to take the magnitude of the reconstructed image for display.

A universal backprojection reconstruction algorithm was implemented [22] for photoacoustic image reconstruction. For the PAUS combined images, all 256 elements were used for receiving signals for both modalities. The Verasonics VDAS I system allows for 128 receive elements per acquisition, and thus two laser pulses are necessary to receive data from 256 elements.

This PAT-UST setup is similar to that of Merčep *et al.* [20], [26]; however, the reconstruction techniques differ. For UST, we both implemented delay-and-sum techniques; however, as stated previously, Merčep *et al.* [20], [26] utilized incoherent spatial compounding, whereas we implemented S-sequence encoding with coherent summation. For PAT, Merčep *et al.* [20], [26] used model-based inversion, which usually includes a deconvolution step that improves resolution. We used universal backprojection, but did not include a deconvolution step. Although deconvolution steps could be included to improve resolution, this will be at the expense of SNR. Because the purpose of this paper is to preform high SNR imaging, we chose to favor SNR over spatial resolution in our reconstruction techniques, and therefore did not include the deconvolution step.

IV. Results

A. Resolution

1) UST Resolution: To characterize spatial resolution, an aluminum wire target (diameter = 12.5 μm, Secon Metals) was suspended in water, orthogonal to the imaging plane. Both STA and S-sequence UST data were collected. Resolution was calculated by taking full-width at half-maximum (FWHM) of the wire targets at six different angles around the target. The wire was placed in seven different places within the imaging field. Close to the center, the resolution was calculated to be 100 ± 36 μm for STA and 119 ± 37 μm for S-sequence imaging. As the wire moved from the center, the FWHMs increased. The average FWHM throughout the plane, however, was measured to be 138 ± 48 μm for STA and 139 ± 44 μm

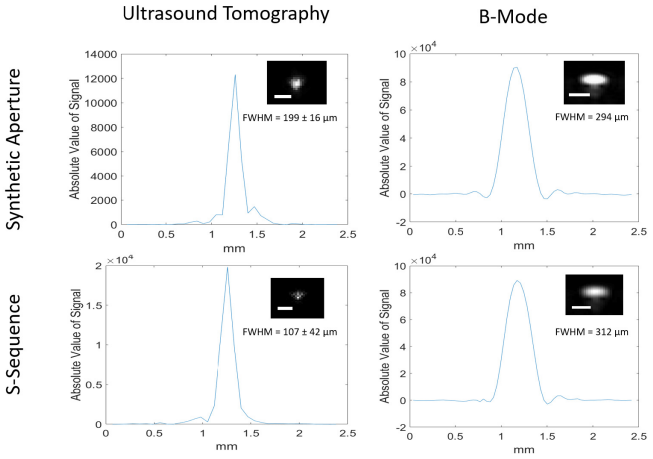

Fig. 2. FWHMs of STA- and S-sequence wire targets from both UST and B-mode linear imaging. Scale bar is equal to 0.5 mm.

for S-sequence, still comparable with the theoretical half-wavelength diffraction limit of our system, which is 150 μm.

To show the improvement over B-mode images, we compared the resolution of our system to a 5-MHz 50% $-$6-dB bandwidth 128-element linear transducer (ATL L7-4, Broadsound Corporation) using both STA- and S-sequence-based imaging techniques on the same wire setup. It can be seen in Fig. 2 that B-mode image lateral resolution was about $2\times$ larger than what we were able to achieve with UST, both when using STA and S-sequence techniques.

While our UST resolutions does not quite compare with the high-frequency linear array counterparts (where they are able to achieve resolutions of 30 μm for a 50-MHz center frequency linear transducer), their penetration depth is limited owing to the high-frequency attenuation. Our system, in contrast, easily images through a 5-cm tissue-mimicking phantom achieving resolutions < 150 μm.

We calculated our out-of-plane resolution by imaging a small needle lowered into the field of view of our system. An edge spread function was then formed, with which we calculated the out-of-plane FWHM by taking the 10%–90% edge response. We found this to be equal to 1.69 mm, which

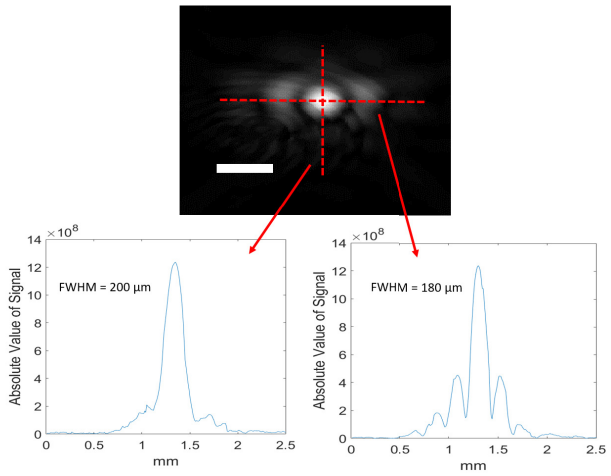

Fig. 3. PAT resolution cross sections with their respective point spread functions. Scale bar is equal to 0.25 mm.

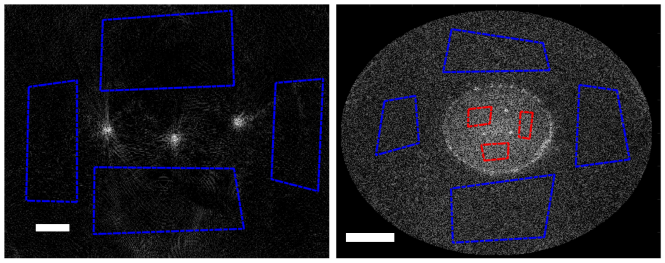

Fig. 4. Noise kernels (blue) and CNR kernels (red) used for SNR and CNR calculation for wire experiment (left) and phantom experiment (right). Scale bar is equal to 5 (left) and 10 mm (right).

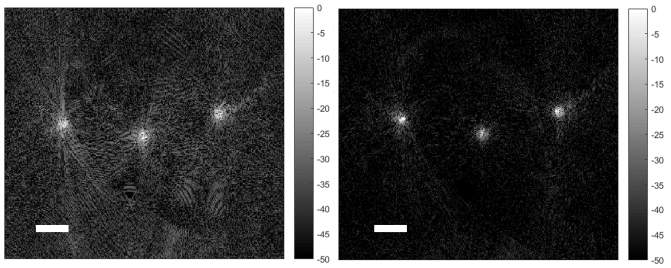

Fig. 5. STA-UST (left) and S-sequence UST (right) on wire targets, with a dynamic range of 50 dB for both images. Scale bar is equal to 5 mm.

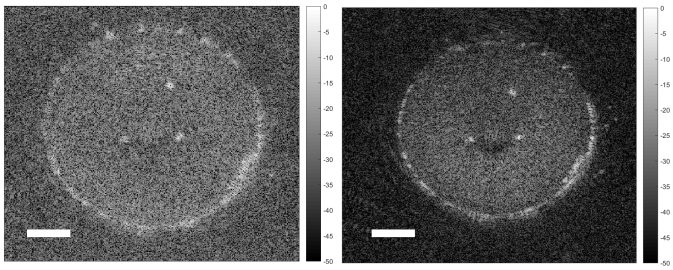

Fig. 6. Ultrasound tomographic images of wire phantom using STA reconstruction (left) and S-sequence reconstruction (right) with a dynamic range of 50 dB for both images. Scale bar is equal to 5 mm.

TABLE I
CNR OF RED KERNELS IN FIG. 4

CNR Kernel	STA	S-Sequence	Improvement
Top left	$-2.36 \pm 0.7dB$	$-0.99] \pm 0.5dB$	$1.4 \pm 0.2dB$
Bottom	$-1.86 \pm 0.6dB$	$0.67 \pm 0.3dB$	$2.5 \pm 0.4dB$
Right	$-2.4 \pm 0.7dB$	$0.0 \pm 0.4dB$	$2.4 \pm 0.4dB$

is comparable with the predicted value of 1.6 mm [calculated as $(1.4)(f\#)(\lambda) = (1.4)(3.7)(0.3\text{ mm})$].

2) PAT Resolution: PAT imaging resolution near the center of the imaging system was reported as 180 ± 32 μm, comparable with a commercial counterpart [20]. FWHMs and an image of the wire target can be seen in Fig. 3. As with UST, PAT resolution degraded as the wire was placed farther away from the center of the transducer, with an average resolution of 189 ± 63 μm.

B. SNR Improvement

To evaluate imaging performance of the UST system with STA and S-sequence methods, three wires (diameter 400 μm) were placed within a water bath normal to the transducer's imaging plane. These wire target images can be seen in Fig. 5. SNR was calculated as $SNR = 20\log_{10}(S_{\max}/\sigma_{\text{noise}})$, where $S_{\max}$ is the maximum reconstructed signal amplitude of the wires and σ_{noise} is the standard deviation of the reconstructed noise. We used four noise kernels for SNR calculation, whose placement can be seen in Fig. 4. We were able to measure SNR as 43.6 ± 1.1 dB for STA and 53.2 ± 1.3 dB for S-Sequence, equaling an increase of 9.6 ± 1 dB.

SNR improvement was also tested on tissue-mimicking phantoms. The phantoms consisted of three wires (diameter 400 μm) placed within a small 10% (w/w) cornstarch and 10% (w/w) gelatin phantom (diameter 3 cm) that was placed at the center of the ring array. Clear gelatin was placed between this phantom and the ring array in order to ensure a more constant speed of sound. Salt water with a ~ 50 g/L salinity could also enable this speed of sound matching [34]–[36]. STA imaging and S-sequence imaging were performed, both averaged 50x. We utilized four noise kernels and three CNR kernels, which can be seen in Fig. 4. Resulting images are shown with a gray map in Fig. 6.

For the phantom experiments, SNR was calculated as before. We were able to measure SNR as $34\pm$ 1 dB for STA and 45 ± 1 dB for S-sequence, an SNR gain of 11.2 ± 0.3 dB. We also calculated the contrast-to-noise ratio of both phantom images, which can be calculated as $\text{CNR} = |\mu_{\text{roi1}} - \mu_{\text{roi2}}|/(\sigma^2_{\text{roi1}} + \sigma^2_{\text{roi2}})^{1/2}$, with μ_{roi1} signifying the mean inside of the phantom and μ_{roi2} the outside. The measured CNR values for the CNR kernels seen in Fig. 4 can be seen in Table I.

For 63 transmitting elements, the theoretical SNR improvement is calculated to be 16.6 dB. Similar to [31], we were unable to achieve the theoretical S-sequence SNR enhancement for both the wire targets and the phantom experiment. This may be due to acoustic crosstalk (which we verified when using all elements rather than only 64). It could also partly be attributed to element-to-element pulse differences not accounted for by the S-matrix decoding steps.

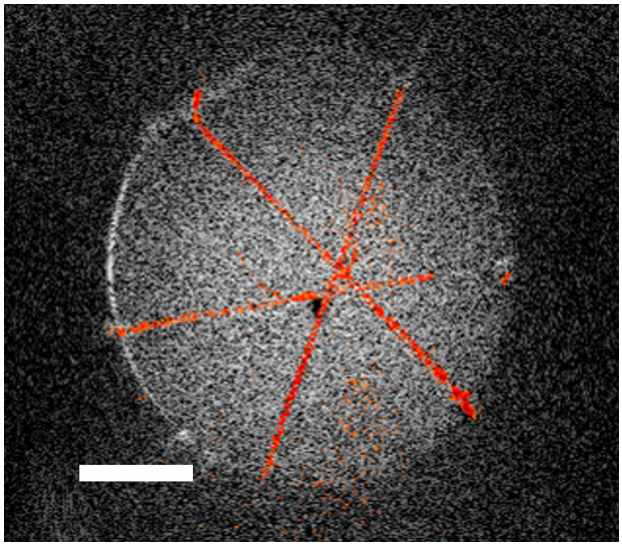

Fig. 7. Photoacoustic/ultrasound composite tomographic images of hair phantom. Red map signifies photoacoustic data and grayscale map signifies ultrasound data. Scale bar is equal to 5 mm.

C. PAUS Composite Imaging

A tissue-mimicking hair phantom (10%w/w gelatin and 10%w/w cornstarch) was created for PAUS composite imaging using 532-nm light. Previous research has shown that cornstarch phantoms act as both an optical and ultrasound scatterer, with an optical scattering coefficient of $\mu_s' = 9.2\ \text{cm}^{-1}$ [37], [38]. A water bath was used as a medium. A PA-US composite image can be seen in Fig. 7, with the photoacoustic data realized with the red map and the ultrasound image consisting of a log-scale gray map with a dynamic range of 40 dB. Both UST and PAT were averaged 50× (using 50 acquisitions for UST and 100 pulses for PAT).

V. Conclusion

We were able to demonstrate the proficiency of S-sequence spatial encoding as a method to boost SNR for STA-based UST reconstructions. Fully coherent STA UST, with and without including the spatial encoding scheme, achieved resolutions that rivaled the theoretic diffraction limit. The combined ultrasound and PAT system may enable new functional and molecular imaging studies in preclinical arenas.

References

[1] L. V. Wang and S. Hu, "Photoacoustic tomography: *In vivo* imaging from organelles to organs," *Science*, vol. 335, no. 6075, pp. 1458–1462, 2012.

[2] J. Yao and L. V. Wang, "Photoacoustic tomography: Fundamentals, advances and prospects," *Contrast Media Molecular Imag.*, vol. 6, no. 5, pp. 332–345, Sep./Oct. 2011.

[3] L. V. Wang, "Prospects of photoacoustic tomography," *Med. Phys.*, vol. 35, no. 12, pp. 5758–5767, Dec. 2008.

[4] R. G. M. Kolkman, P. J. Brands, W. Steenbergen, and T. G. van Leeuwen, "Real-time *in vivo* photoacoustic and ultrasound imaging," *J. Biomed. Opt.*, vol. 13, no. 5, p. 050510, Oct. 2008.

[5] A. B. Karpiouk *et al.*, "Combined ultrasound and photoacoustic imaging to detect and stage deep vein thrombosis: Phantom and *ex vivo* studies," *J. Biomed. Opt.*, vol. 13, no. 5, p. 054061, Oct. 2008.

[6] J. J. Niederhauser, M. Jaeger, R. Lemor, P. Weber, and M. Frenz, "Combined ultrasound and optoacoustic system for real-time high-contrast vascular imaging *in vivo*," *IEEE Trans. Med. Imag.*, vol. 24, no. 4, pp. 436–440, Apr. 2005.

[7] L. G. Montilla, R. Olafsson, D. R. Bauer, and R. S. Witte, "Real-time photoacoustic and ultrasound imaging: A simple solution for clinical ultrasound systems with linear arrays," *Phys. Med. Biol.*, vol. 58, no. 1, p. N1, Jan. 2012.

[8] D. Yang, D. Xing, S. Yang, and L. Xiang, "Fast full-view photoacoustic imaging by combined scanning with a linear transducer array," *Opt. Exp.*, vol. 15, no. 23, pp. 15566–15575, 2007.

[9] G. Jérôme, M. A. Araque, D. Alexander, and N. Vasilis, "Three-dimensional optoacoustic tomography using a conventional ultrasound linear detector array: Whole-body tomographic system for small animals," *Med. Phys.*, vol. 40, no. 1, p. 013302, Jan. 2013.

[10] J. Gamelin *et al.*, "A real-time photoacoustic tomography system for small animals," *Opt. Exp.*, vol. 17, no. 13, pp. 10489–10498, 2009.

[11] J. Xia *et al.*, "Whole-body ring-shaped confocal photoacoustic computed tomography of small animals *in vivo*," *J. Biomed. Opt.*, vol. 17, no. 5, pp. 050506-1–050506-3, Apr. 2012.

[12] A. Buehler, E. Herzog, D. Razansky, and V. Ntziachristos, "Video rate optoacoustic tomography of mouse kidney perfusion," *Opt. Lett.*, vol. 35, no. 14, pp. 2475–2477, 2010.

[13] D. Razansky, A. Buehler, and V. Ntziachristos, "Volumetric real-time multispectral optoacoustic tomography of biomarkers," *Nature Protocols*, vol. 6, no. 8, pp. 1121–1129, 2011.

[14] R. B. Lam *et al.*, "Dynamic optical angiography of mouse anatomy using radial projections," *Proc. SPIE*, vol. 7564, p. 756405, Feb. 2010.

[15] R. Kruger *et al.*, "HYPR-spectral photoacoustic CT for preclinical imaging," *Proc. SPIE*, vol. 7177, p. 71770F, Feb. 2009.

[16] N. Duric *et al.*, "Breast ultrasound tomography: Bridging the gap to clinical practice," *Proc. SPIE*, vol. 8320, p. 83200O, Feb. 2012.

[17] M. Birk, M. Zapf, M. Balzer, N. Ruiter, and J. Becker, "A comprehensive comparison of GPU- and FPGA-based acceleration of reflection image reconstruction for 3D ultrasound computer tomography," *J. Real-Time Image Process.*, vol. 9, no. 1, pp. 159–170, Mar. 2014.

[18] C. Li, G. S. Sandhu, O. Roy, N. Duric, V. Allada, and S. Schmidt, "Toward a practical ultrasound waveform tomography algorithm for improving breast imaging," *Proc. SPIE*, vol. 9040, p. 90401P, Mar. 2014.

[19] B. Ranger *et al.*, "Breast imaging with ultrasound tomography: A comparative study with MRI," *Proc. SPIE*, vol. 7629, p. 762906, Mar. 2010.

[20] E. Mercep, G. Jeng, S. Morscher, P.-C. Li, and D. Razansky, "Hybrid optoacoustic tomography and pulse-echo ultrasonography using concave arrays," *IEEE Trans. Ultrason., Ferroelect., Freq. Control*, vol. 62, no. 9, pp. 1651–1661, Sep. 2015.

[21] N. V. Ruiter, M. Zapf, T. Hopp, R. Dapp, and H. Gemmeke, "Phantom image results of an optimized full 3D USCT," *Proc. SPIE*, vol. 8320, p. 832005, Feb. 2012.

[22] M. Xu and L. V. Wang, "Universal back-projection algorithm for photoacoustic computed tomography," *Phys. Rev. E, Stat. Phys. Plasmas Fluids Relat. Interdiscip. Top.*, vol. 71, no. 1, p. 016706, Jan. 2005.

[23] J. R. Rajian, G. Girish, and X. Wang, "Photoacoustic tomography to identify inflammatory arthritis," *J. Biomed. Opt.*, vol. 17, no. 9, pp. 096013-1–096013-6, Sep. 2012.

[24] G. Ku, X. Wang, G. Stoica, and L. V. Wang, "Multiple-bandwidth photoacoustic tomography," *Phys. Med. Biol.*, vol. 49, no. 7, p. 1329, 2004.

[25] C. Haisch, "Quantitative analysis in medicine using photoacoustic tomography," *Anal. Bioanal. Chem.*, vol. 393, no. 2, pp. 473–479, Jan. 2009.

[26] E. Merčep, N. C. Burton, J. Claussen, and D. Razansky, "Whole-body live mouse imaging by hybrid reflection-mode ultrasound and optoacoustic tomography," *Opt. Lett.*, vol. 40, no. 20, pp. 4643–4646, 2015.

[27] A. Needles *et al.*, "Development and initial application of a fully integrated photoacoustic micro-ultrasound system," *IEEE Trans. Ultrason., Ferroelect., Freq. Control*, vol. 60, no. 5, pp. 888–897, May 2013.

[28] M. Lakshman and A. Needles, "Screening and quantification of the tumor microenvironment with micro-ultrasound and photoacoustic imaging," *Nature Methods*, vol. 12, no. 4, Mar. 2015.

[29] *MX Transducers*, accessed on Nov. 7, 2016. [Online]. Available: http://www.visualsonics.com/products/vevo-3100/mx-transducers

[30] H. Gemmeke and N. V. Ruiter, "3D ultrasound computer tomography for medical imaging," *Nucl. Instrum. Methods Phys. Res. A, Accel. Spectrom. Detect. Assoc. Equip.*, vol. 580, no. 2, pp. 1057–1065, Oct. 2007.

[31] T. Harrison, A. Sampaleanu, and R. Zemp, "S-sequence spatially-encoded synthetic aperture ultrasound imaging [Correspondence]," *IEEE Trans. Ultrason., Ferroelect., Freq. Control*, vol. 61, no. 5, pp. 886–890, May 2014.
[32] R. J. Zemp, A. Sampaleanu, and T. Harrison, "S-sequence encoded synthetic aperture B-scan ultrasound imaging," in *Proc. IEEE Int. Ultrason. Symp. (IUS)*, Jul. 2013, pp. 593–595.
[33] E. Kretzek, M. Zapf, M. Birk, H. Gemmeke, and N. V. Ruiter, "GPU based acceleration of 3D USCT image reconstruction with efficient integration into MATLAB," *Proc. SPIE*, vol. 8675, pp. 86750O-1–86750O-10, Mar. 2013. [Online]. Available: http://dx.doi.org/10.1117/12.2007184
[34] C. C. Leroy, S. P. Robinson, and M. J. Goldsmith, "A new equation for the accurate calculation of sound speed in all oceans," *J. Acoust. Soc. Amer.*, vol. 124, no. 5, pp. 2774–2782, 2008.
[35] N. Bilaniuk and G. S. K. Wong, "Speed of sound in pure water as a function of temperature," *J. Acoust. Soc. Amer.*, vol. 93, no. 3, pp. 1609–1612, 1993.
[36] S. J. Kleis and L. A. Sanchez, "Dependence of sound velocity on salinity and temperature in saline solutions," *Solar Energy*, vol. 46, no. 6, pp. 371–375, 1991.
[37] R. J. Zemp, C. Kim, and L. V. Wang, "Ultrasound-modulated optical tomography with intense acoustic bursts," *Appl. Opt.*, vol. 46, no. 10, pp. 1615–1623, Apr. 2007. [Online]. Available: http://ao.osa.org/abstract.cfm?URI=ao-46-10-1615
[38] C. Kim, A. Garcia-Uribe, S.-R. Kothapalli, and L. V. Wang, "Optical phantoms for ultrasound-modulated optical tomography," *Proc. SPIE*, vol. 6870, p. 68700M, Feb. 2008.

Quinn M. Barber (S'16–A'16) was born in Lethbridge, AB, Canada. He received the B.Sc. degree in engineering physics (with distinction) from the University of Alberta, Edmonton, AB, where he is currently pursuing the M.Sc. degree in electrical and computer engineering with Dr. R. J. Zemp's group.

His current research interests include photoacoustic and ultrasound imaging, specializing in tomographic reconstruction.

Roger J. Zemp (S'04-M'04) was born in Calgary, AB, Canada, in 1974. He received the B.Sc. degree in physics from the University of Alberta, Edmonton, AB, Canada, in 1998, the M.A.Sc. degree in electrical and computer engineering from the University of Toronto, Toronto, ON, Canada, in 2000, and the Ph.D. degree in biomedical engineering from the University of California, Davis, CA, USA, in 2004.

He was a Post-Doctoral Fellow at Texas A&M University, College Station, TX, USA, from 2004 to 2006, then at Washington University, St. Louis, MO, USA, from 2006 to 2007. He is currently an Associate Professor with the Department of Electrical and Computer Engineering, University of Alberta. His current research interests include ultrasound imaging, biomedical optics, and photoacoustic imaging.